AERODYNAMIC INTERACTION BETWEEN WING AND TRUSS IN TRANSONIC FLOW

S.K. Siemons, BSc

University of Tokyo, Graduate School of Engineering, Department of Aeronautics and Astronautics, Rinoie and Imamura Lab.

Prof.dr.ir. K. Rinoie
dr.ir. T. Imamura

University of Twente, Faculty of Engineering Technology, Engineering Fluid Dynamics

Prof.dr.ir C.H. Venner
Prof.dr.ir H.W.M. Hoeijmakers

24 June 2015

Abstract

Two-dimensional calculations on biplanes in transonic flow are presented. The effect of stagger was investigated on biplanes with equal chord length and angle of attack, with the gap equal to the chord length.

A finite volume method was used to solve the Euler equations on a quadtree Cartesian grid. A multi-level approach to solution-based grid refinement is presented to refine the grid at shockwaves. The airfoils under study are the symmetric NACA0012 and the supercritical RAE2822. For these airfoils the flow was calculated for the free stream Mach numbers $M_\infty = 0.4, 0.5, 0.6, 0.7, 0.8$ and angle of attack $\alpha = 0°, 2°, 4°, 6°, 8°$.

It was observed that the flow chokes when the airfoils are positioned such that a duct is formed by the overlapping surfaces. The duct then has a geometry similar to a convergent-divergent nozzle. The transition from subcritical flow to supercritical flow, i.e. choked flow, occurs at subcritical flow conditions of the single airfoil. At higher free stream velocity the choked flow changed into to another flow pattern for positive staggered configurations only. The new flow pattern is characterised by an upward angled oblique shockwave at the trailing edge of the upper airfoil followed by a detached normal shockwave. The normal shock connects to the upper surface of the lower airfoil.

In case of choked flow the lift and drag are affected in two distinct ways. Firstly, the early transition to supercritical flow increases the drag in comparison with the single airfoil and other biplane configurations. Secondly, the lifting capabilities of both airfoils is decreased because the flow in the duct is almost symmetrical with respect to the upper and lower walls of the duct. The transition from choked flow to a detached normal shock is not observed in the drag polar.

Nomenclature

A	nondimensional throat cross section
C_d	drag coefficient
C_l	lift coefficient
C_m	quarter chord moment coefficient
C_p	pressure coefficient
c	chord length (reference length)
F	functional C_l, C_d, C_m
H	nondimensional height of a refinement box
h	nondimensional cell size
i, j, n	ghost cell node number
L_1, L_2, L_∞	L-1, L-2, L-infinity norm
L_{max}	convergence threshold for L_1, L_2
M	Mach number
N	total number of cells
p	pressure, order of accuracy
R	symmetry line of flow expansion
T	total number of iterations
t	airfoil thickness, iteration number
u	velocity in x direction
v	velocity in y direction
x	direction from leading edge to trailing edge of main-wing
x_0	nondimensional stagger
y	direction from lower to upper surface of main-wing
y_0	nondimensional gap
W	nondimensional width of a refinement box
α	angle of attack
ω	wall cell size ratio
ρ	density
$\#_{airfoil}$	number of data points of airfoil
$\%_{max}$	convergence threshold for percentage change in functionals

Superscript

f, m, c	fine, medium, coarse grids
$*$	$h_w \rightarrow 0$ grid

Subscript

b, w	refinement box and wall cells
DD	drag divergence
∞	free stream condition

1. Introduction

The truss-braced wing configuration (TBW) is a conceptual aircraft with the main-wing positioned on top of the fuselage. Additional members connect the main-wing to the bottom of the fuselage to stiffen the wing pattern. These members are referred to as the trusses and reduce the bending moment in the wing, thus allowing for a reduced thickness-over-chord ratio t/c. This translates to a reduction in main-wing chord and spar thickness, and therefore a reduced chord Reynolds number. The reduced wing thickness results in decreased wave drag as elaborated by Meadows et al. (1).

The SUGAR program is a NASA contract awarded to Boeing for research into subsonic commercial aircraft technology to meet the agency's future environmental and efficiency goals in the 2030-2050 time frame. Through a partnership with General Electric, Georgia's Tech Aerospace System Design Laboratory, Virginia Tech and NextGen Aeronautics, Boeing currently is studying two concept aircraft: the SUGAR Volt, run by hybrid electric propulsion, and the SUGAR Freeze, powered by liquefied natural gas. The SUGAR program has identified potential fuel savings for the TBW, which, according to Boeing (2), could produce a 5 percent to 10 percent improvement in fuel consumption over the conventional cantilever wing configurations of today.

Airbus is has patented (3) a TWB concept with forward swept trusses creating a lambda-box wing configuration. This configuration has a vertical wing between the main-wing and the truss such that stagger and gap is maintained at the connection.

Recent aerodynamic analysis of the TBW aircraft using a conceptual vortex-lattice aerodynamic tool VORLAX coupled with the aerodynamic superposition method was presented by Ting et al. (4). Based on the underlying linear potential flow theory, the principle of aerodynamic superposition is leveraged to deal with a complex shape such as the TBW. The aerodynamic superposition showed good agreement with CFD results computed by FUN3D and USM3D. Because the vortex-lattice method is based in potential flow theory, it is an inviscid code that can only compute inviscid drag due to lift, and cannot predict viscous or wave drag.

In the work of Hwang et al. (5) a locally implicit total variation diminishing scheme is used to solve the two-dimensional Euler equations. An unstructured triangular grid was generated around a biplane. It was found that although the flow condition is subcritical for the single airfoil, the biplane configuration developed a shockwave between the two airfoils.

This report presents a study on the aerodynamic interaction of the main-wing and truss in transonic flow. By solving the two-dimensional Euler equations the inviscid drag due to lift and the wave drag is calculated for various configurations of the main-wing and truss. Two airfoils are investigated: the symmetric NACA0012 and the supercritical RAE2822 airfoil. For both airfoils the effect of stagger is investigated, and for the RAE2822 airfoil the effect of the gap with zero-stagger is also investigated. Even at the low accuracy flow transitions are observed when increasing the free stream Mach number from $M_\infty = 0.4$ to $M_\infty = 0.8$. This allows for a rough understanding of the effects that must be dealt with in the design of the TBW in transonic flow.

The structure of this report is as follows. In Section 2 the numerical methods of the flow solver are discussed, together with a solution-based grid refinement method to refine the grid at the shockwaves. Higher order estimates of the functionals are used to determine the cell size in the study. In Section 3 the drag divergence Mach number is investigated for both single airfoils and biplane configurations for variable stagger and gap. The results are discussed in Section 4 and the conclusions given in Section 5. In Appendix I and II to drag polar plots of the biplane configurations are given for the NACA0012 and RAE2822 airfoils respectively. The flow fields of all the calculations are not found in this report, since they include over 900 cases.

2. Methods

Biplane configurations and flow conditions

Two different airfoils are investigated, both in subcritical and supercritical conditions. The first airfoil is the symmetric NACA0012, which has been adjusted with a sharp trailing edge. The second airfoil is the supercritical RAE2822 airfoil.

Consider the biplane configuration shown in Figure 1. Following the TBW description, the upper and lower airfoils are the main-wing and truss respectively. The stagger x_0 is defined as the nondimensional distance between the leading edges of the main-wing and truss. Positive stagger indicates that the truss is located behind the main-wing with respect to the flow direction. The nondimensional gap y_0 is the vertical distance between the leading edges of the main-wing and truss. A negative gap indicates that the truss is positioned below the main-wing. In this study the main-wing and truss are placed parallel in the flow and both have chord length c. Both the stagger and gap are made dimensionless with the chord length.

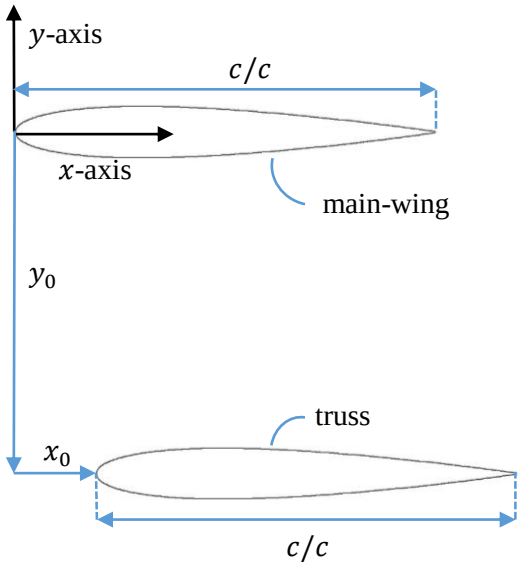

Figure 1. Dimensionless coordinate system of the biplane configurations used in the present study.

The biplane configurations and flow conditions under consideration for the NACA0012 biplane are as follows:

$$x_0 = \pm 10, \pm 2, 0$$
$$y_0 = -1$$
$$c/c = 1$$
$$M_\infty = 0.4, 0.5, 0.6, 0.7, 0.8$$
$$\alpha = 0°, 2°, 4°, 6°, 8°$$

The RAE2822 biplane is investigated in two steps. First, the stagger is varied with smaller increments since the NACA0012 biplane showed no interaction for $|x_0| \geq 2$:

$$x_0 = \pm 1, \pm 0.5, \pm 0.25, 0$$
$$y_0 = -1$$
$$c/c = 1$$
$$M_\infty = 0.4, 0.5, 0.6, 0.7, 0.8$$
$$\alpha = 0°, 2°, 4°, 6°, 8°$$

Second, the effect of the gap is investigated at zero stagger:

$$x_0 = 0$$
$$y_0 = -1.5, -1, -0.75, -0.5, -0.25$$
$$c/c = 1$$
$$M_\infty = 0.4, 0.5, 0.6, 0.8$$
$$\alpha = 0°, 2°, 4°$$

With this set the transition from subsonic to transonic flow can be investigated for various biplane configurations. These include cross-sections of the TBW designs presented by Nam et al. (6), Chakrabotry et al. (7) and the lambda-box wing presented by Airbus (3).

Numerical methods of the flow solver

A cell-centered finite volume method is used to solve the two-dimensional Euler equations on a Cartesian quadtree structured grid with immersed boundary method (8). The MUSCL scheme with third order accuracy (9) is used for the spatial discretization and the numerical flux is evaluated using the SLAU scheme (10) together with the Van Albada flux limiter. The LU-SGS implicit method is used for solving the time integration system with local time stepping.

Grid generation

The grid is generated around the airfoils by the solver. In the quadtree grid all cells are squares with variable size h which is made dimensionless with the chord length c. The smallest cells are placed at the surface of the airfoils. These cells are called wall cells and have size h_w. The other cells are called fluid cells and have a variable size depending on the location in the grid. The cell size in the quadtree grid in this study grows as follows. At least one adjacent wall and fluid cell are required before the third cell is allowed to double in size. Subsequently at least three adjacent fluid cells are required before a fourth fluid cell is allowed to double in size. At the interface of two small cells and one large cell a hanging node is found. This is the node that the two smaller cells share, but is not shared with the larger cell. The total number of cells is denoted with N. Rectangular grid refinement boxes with width W and height H can be specified in which the cell size is kept equal or lower to h_b. As an example Figure 2 shows the grid generated around a unit circle with a square refinement box centered at the leading edge of the circle. The refinement box has a height and width $H = W = 1$ and both the wall cell size and refinement box cell size is $h_w = h_b = 0.01$. The result is that the cells at the surface of the circle and in the refinement box are equally small, and that the cell size of the other cells is proportional with the distance away from the body and refinement box.

The flow solver and grid generator is developed by the Rinoie and Imamura Laboratory of the Department of Aeronautics and Astronautics at the University of Tokyo. The solver supports the Navier-Stokes

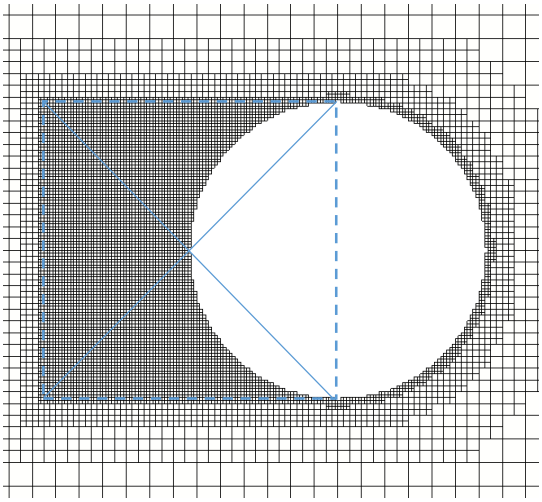

Figure 2. Quadtree grid around a unit circle with a square refinement box centered at the leading edge of the circle with $H = W = 1$ and $h_w = h_b = 0.01$.

equations and a turbulence model. A bug in the grid generator was repaired, which always activated the turbulence model. The fix reduced the computational time to generate the grid significantly. The solver performs T number of iterations specified beforehand by the user. After every iteration t the solver stores the aerodynamic coefficients C_d, C_L and C_m of the airfoils, together with the L_1, L_2 and L_∞ norms of the residuals. After finishing the T iterations the calculated cell variables $\rho, u, v, p, C_p, M_\infty$ are stored. These signify the density, velocity in x- and y-direction, pressure, dimensionless pressure coefficient and Mach number respectively at the cell centre.

A multi-level approach to solution-based grid refinement

In the following subsections the grid refinement method is presented. In the first subsection the shockwaves in transonic flow around airfoils are analysed, followed by a discussion on the necessity to refine the grid at shockwaves in quadtree grids. In the next subsection, a shock detection method is presented which is developed for quadtree grids. The shock detection method flags cell interfaces on which refinement boxes are placed. A multi-level approach to the grid refinement method is presented at the last subsections

Shockwaves in transonic flow

A shockwave is a flow phenomenon through which supersonic flow is decelerated such that the tangential velocity component remains constant across the shock. In this study shockwaves are classified according to two distinct features: the orientation with respect to the flow direction and the exit velocity respectively. Based on the orientation, shocks are classified as either normal or oblique shocks. Normal shocks are orientated perpendicular to the flow direction and thus the tangential velocity component is zero. Oblique shocks are inclined to the flow direction and thus the tangential component is not zero. The second classification is based on the exit velocity behind the shock, and classifies shocks as either strong or weak. A strong shock decelerates the flow from supersonic to subsonic velocity. A weak shock decelerates supersonic flow but the exit velocity remains supersonic. A normal shock is always a strong shock, while an oblique shock can be either a strong or weak shock.

In transonic flow around airfoils a normal shock is seen at the back-side of the supersonic regions. An oblique shock on the other hand is not seen transonic flow around airfoils, but is often associated with supersonic flow around sharp bodies, or supersonic flow in a curved duct. The shock detection method thus must be able to detect normal or strong shockwaves, which are found at the back-side of the supersonic region.

Uncertainty in the quadtree grid

Consider a sufficiently accurate solution on a grid around a slender body in transonic flow at small angle of attack. At every cell it is then assumed that the velocity in x-direction is much larger than the velocity in y-direction:

$$u \gg v \tag{1}$$

Therefore the flow can locally be considered as one-dimensional flow. In this grid consider two cells, adjacent in x-direction, with supersonic and subsonic velocity respectively. The flow then decelerates from supersonic to subsonic velocity somewhere between these cell centres through a normal shock, which is forced on the cell interface. The cell size in the default quadtree grid is proportional with the square of the distance away from the body, and thus the determination of the shockwave at remote cells is not accurate. This shows the necessity to refine the grid at those remote locations of uncertainty.

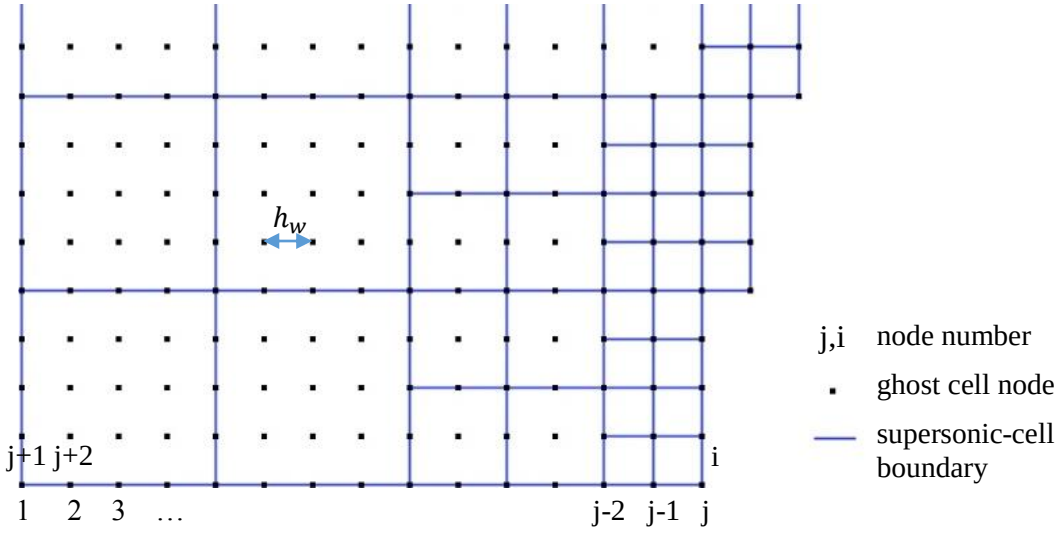

Figure 3. Ghost cell numbering to detect the back-side of the supersonic area. The blue lines indicate the boundary of supersonic cells, the black dots indicate the nodes of the ghost cells and the node number is shown below the corresponding node.

Solution-based grid refinement

The flow solver does not support grid refinement during a calculation, and thus a solution-based grid refinement method is used. The grid refinement method was adapted from De Zeeuw et al. (11). In their solution-based grid refinement method cells are selected for grid refinement, and also coarsening, based on the velocity percentage difference between two adjacent cells. In the present study cell interfaces on which a strong shockwave is detected are selected for grid refinement.

Shock detection

Strong shocks are in the present method detected based on the cell Mach numbers of the solution. This method can be considered an image analysis method, as described by Kanamori (12).

An algorithm is developed to trace the back-side of the supersonic regions. The algorithm works as follows. The cells with Mach number larger than 1 are selected and split into ghost cells with length h_w. This removes the hanging nodes and makes all cells equally sized. The ghost cell node coordinates are stored in a list which is ordered on the value of the y-coordinate, and subsequently on the value of the x-coordinate of the nodes. The result is that the first node in the list has the smallest x- and y-coordinates. The second node has the same y-coordinate, but has the second smallest x-coordinate. The next node has again the same y-coordinate and the next smallest x-coordinate until all the nodes with the lowest y-coordinate are numbered. The numbering is continued with the node with second smallest y-coordinate and the smallest x-coordinate etc. This numbering is illustrated in Figure 3. The numbering starts on the left node of the lowest row with node numbers 1,2,3, ... until the last node of the first row has number j. The numbering is continued from left to right on the row above with $j+1, j+2,$ ... until the last node on the second row has number i. This numbering is continued until the last node has both the largest y- and x-coordinate. The nodes are swept from the first to the second last and a shock is detected if either:

$$x_{n+1} - x_n > h_w \ \wedge y_{n+1} = y_n \qquad (2)$$

or

$$y_{n+1} > y_n \qquad (3)$$

where x_n and y_n signify the x- and y-coordinate of the node number n. When sweeping through the nodes these two criteria signify respectively 1) the back-side of a supersonic region while another supersonic region still exist on the same y-coordinate and 2) the back-side of the last supersonic region at that y-coordinate. When a shock is detected the corresponding node is selected for refinement. The result is that all the cell interfaces at which a strong shock occurs are described by their selected ghost node coordinates.

Refinement method

After the shock detection a new grid is generated with square refinement boxes centered at the coordinates of the flagged nodes. The flagged nodes are an inaccurate determination of the shockwave, hence the grid refinement, and therefore multiple grid refinement iterations are inherently required. In this study the refinement boxes have a length $4h_w$ and the maximum cell size in the box is $h_b = h_w$. This refines the cells at the shockwave up to the wall cell size in a single refinement iteration. It is also possible to refine the cell size in the refinement boxes through multiple steps, for example by choosing h_b to be $4h_w, 2h_w$ and h_w for every step respectively. The latter method could be faster in fine grids, but was not used.

Multi-level approach

A different method to decrease the computational time was developed using two properties of the solver. Firstly, the computational time required to generate the quadtree grid is negligible to the computational time required for solving the flow. Secondly, the computational time required for solving the flow is proportional to the square of the total number of cells. Calculations on coarse grids are therefore a very cheap way to obtain the initial predictions of the shockwave. The grid refinement is then applied to a medium grid. The solution on the medium grid is refined again and the new grid refinement is applied to a fine grid and so on. The flow solution of a higher level is thus essentially used for grid refinement on a lower level. This multi-level approach to solution-based grid refinement showed a significant reduction in computational time.

Solution and refinement convergence

After the solver finishes the T iterations the solution is evaluated. The L_1 and L_2 norms of the residuals are a measure of the overall quality of the solution on the grid. If the norms are machine zero the solution cannot be improved any further. This accuracy however requires a very large computational time. It was found that a threshold of $L_{max} = 10^{-8}$ for the L_1 and L_2 norms resulted in a convergence of the functionals C_d, C_L and C_m within 0.01 percentage change. If the norms were higher than the threshold an additional T iterations were performed. Some calculations showed an early convergence of the L_1 and L_2 norms. This was identified by comparing the L_1 and L_2 norms of the last iteration with an earlier iteration. It was found that in some cases of this early convergence, a shockwave was frozen on an inaccurate cell interface of a fine and larger cell. The norms of the residuals therefore convergence to a relative high value. The freezing of the shockwave is probably related with the time integration scheme in combination with the transition from a fine cell to a larger cell.

To determine if the grid refinement is placed at the correct location the functionals C_d, C_L and C_m of the last two computations are compared. If the percentage change of all the functionals of the last computation is lower than $\%_{max}$ the grid refinement is sufficiently accurate and it is sent to the next level. It was found that if $\%_{max} \leq 0.01$ the grid refinement was successfully placed at the shockwave.

The solution and grid refinement evaluation is automated such that for every flow condition and biplane configuration the final solution is calculated without human intervention.

Higher order estimates of functionals

The multi-level approach calculates solutions on multiple levels, which are used for a higher order prediction of the aerodynamic coefficients. Following the work of Xing et al. (13) the limiting value F^* of the functionals C_d, C_L and C_m can be estimated as $h_w \rightarrow 0$:

$$F^* = F^f + \frac{F^f - F^m}{\omega^p - 1} \tag{4}$$

$$\omega = \frac{h_w^m}{h_w^f} = \frac{h_w^c}{h_w^m} \tag{5}$$

$$p = \ln\left(\frac{F^c - F^m}{F^m - F^f}\right) / \ln(\omega) \tag{6}$$

Here the superscript f, m, c denote the fine, medium and coarse grid, ω the ratio between the wall cell size of the grids and p the order of accuracy. Note that in equation (4) ω^p signifies ω raised to the power p. This extrapolation is called the 3-point Richardson extrapolation.

The effect of the functional errors on the estimate of order of accuracy is neglected as elaborated by Vassberg (14). The family of

grids is arguably not suitable for Richardson extrapolation due to the uncontrollable grid refinement but any effects on the order of accuracy are also neglected.

Test cases and wall cell size

The higher order estimate is used to determine the wall cell size for the biplane calculations. In addition the higher order estimates were used to validate the solver and grid refinement method.

Starting with a wall cell size of $h_w = 0.01$ calculations on a single NACA0012 airfoil were conducted. The wall cell size was halved between every grid level until $h_w = 0.0003125$. This created a family of grids consisting of 6 levels with $\omega = 2$. Nonlifting and lifting test cases at both subcritical and supercritical flow were investigated. The choice of this set of flow conditions allowed the ability to investigate: 1) drag with and without lifting effects, 2) drag with and without shock effects. The matrix of flow conditions under consideration is provided in Table 1.

M, α	Nonlifting	Lifting
Subcritical	$M_\infty = 0.5$ $\alpha = 0°$	$M_\infty = 0.5$ $\alpha = 1.25°$
Supercritical	$M_\infty = 0.8$ $\alpha = 0°$	$M_\infty = 0.8$ $\alpha = 1.25°$

Table 1. Matrix of flow conditions used for the test cases.

In Figure 4 the drag coefficients of the supercritical lifting case are shown as function of the wall cell size. The Richardson extrapolation is also shown, with a $\pm 2.5\%$ margin. For this case the asymptotic range is not reached, but the last extrapolated value for C_d is within 2.5% of the second last. Therefore the limited value of C_d^* as $h_w \to 0$ is expected to be within a $\pm 2.5\%$ margin of the last extrapolation. The results of the other test cases showed similar results, with at least the last two extrapolations within a $\pm 2.5\%$ margin. From these results it was concluded that solutions with a wall cell size of $h_w = 0.00125$ are within 33% accuracy. The Richardson extrapolation of the functionals is not used in the results of the biplane and single airfoil calculations because based on these findings the extrapolated functionals are inaccurate at this wall cell size. The solutions of the medium and

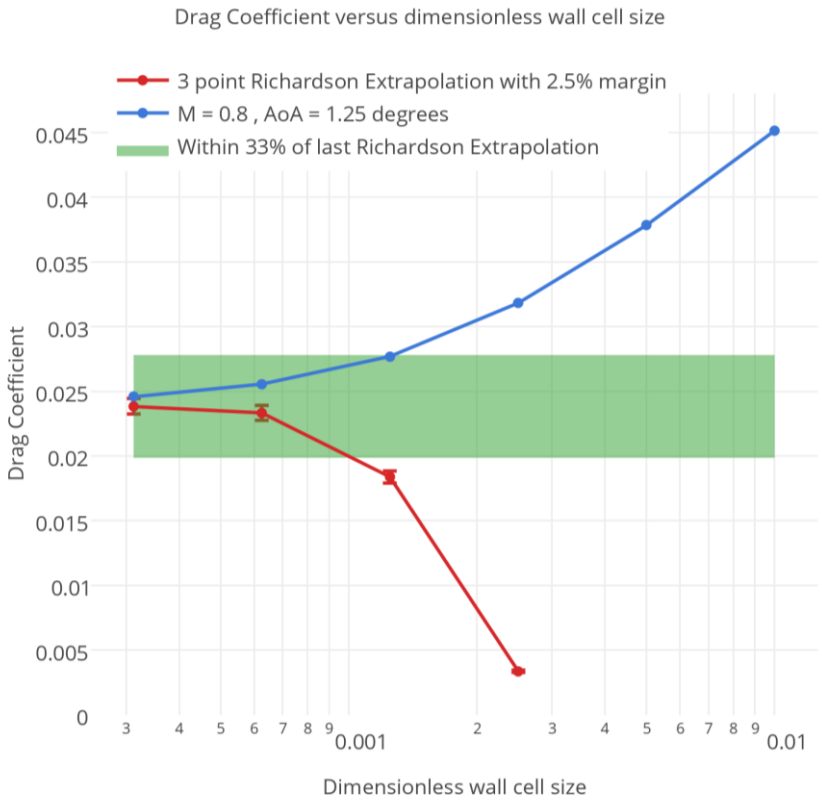

Figure 4. Convergence of calculated drag coefficient and 3-point Richardson Extrapolation on NACA0012 airfoil.

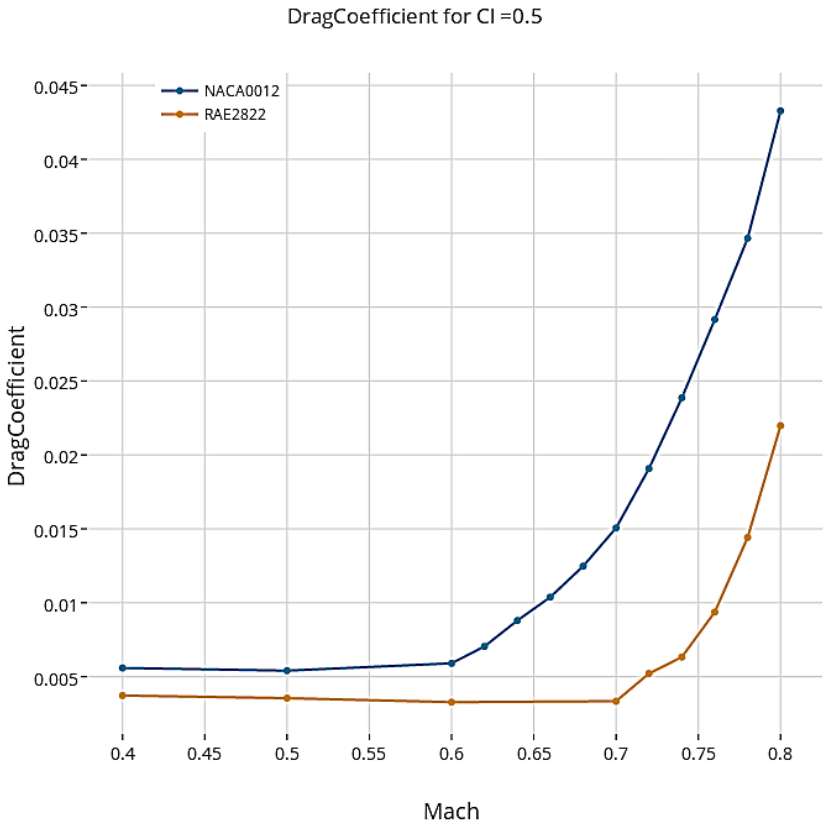

Figure 5. Drag coefficient the NACA0012 and RAE2822 airfoil at constant lift coefficient against Mach number.

coarse grid are not in the asymptotic range because the wall cell size is too large.

3. Results

Single NACA0012

The initial calculations on the NACA0012 airfoil showed a rapid increase in drag between $M_\infty = 0.6$ and $M_\infty = 0.7$ at constant lift. Additional calculations with Mach number increments of $\Delta M_\infty = 0.2$ were performed to locate the Mach drag divergence number more accurately. The drag at constant lift is shown in Figure 5. From the drag polar plots, the drag coefficient is interpolated for lift coefficient of $C_l = 0.5$ at every Mach number. A linear interpolation is used, which introduces small errors in the plot. The results show for subcritical flow condition a drag coefficient of approximately $C_d \approx 0.006$. From $M_\infty = 0.62$ the drag rises, with increasing slope. The drag coefficient at $M_\infty = 0.7$ and $M_\infty = 0.8$ is $C_d \approx 0.015$ and $C_d \approx 0.044$ respectively. At $M_\infty = 0.7$ the drag almost tripled compared to $M_\infty = 0.6$, while at $M_\infty = 0.8$ the drag almost tripled again.

Two definitions of the drag divergence Mach number M_{DD} are found in the book Airplane Aerodynamics and Performance (15): the Boeing and Douglas definition respectively. According to the Boeing definition the drag divergence Mach number is "that free stream Mach number for which the drag due to compressibility first reaches 20 drag counts ($\Delta C_d = 0.0020$) above the incompressible level". According to the Douglas definition the drag divergence Mach number is "that free stream Mach number for which the slope of the dragrise, $\partial C_d / \partial M$, first eaches the value of 0.10". Since the Douglas definition requires a continuous formulation of the drag as function of the Mach number it is not used. Following the Boeing definition the drag divergence Mach number for the NACA0012 airfoil is estimated $0.62 < M_{DD} < 0.64$ at $C_l = 0.5$.

Single RAE2822

The results on the RAE2822 airfoil are also shown in Figure 5. Similar to the NACA0012

airfoil additional calculations were performed to identify the drag divergence Mach number of the RAE2822 airfoil more accurately. These additional calculations are at Mach number $M_\infty = 0.72, 0.74, 0.76, 0.78$.

At $0.4 \leq M_\infty \leq 0.7$ the drag is approximately $C_d \approx 0.004$, which is two-thirds of the drag found for the NACA0012 airfoil. The drag rises for $M_\infty \geq 0.72$ and shows a small bump at $M_\infty = 0.72$. This bump is not due to the linear interpolation of the drag in the drag polar. Following the Boeing definition the drag divergence Mach number is estimated at $0.72 < M_{DD} < 0.74$ for $C_l = 0.5$.

NACA0012 Biplane

The drag polar of the NACA0012 biplane configurations at different Mach number are shown in Appendix I at Figure 12-Figure 16 on pages 1-1. For $0.4 \leq M_\infty \leq 0.6$ the drag polar of the different biplane configurations show no large differences for $0° \leq \alpha \leq 4°$. These are subcritical flow conditions. Note that for subcritical flow the drag polar is a quadratic curve, making the differences smaller than as they would appear in these linear interpolated figures. For $6° \leq \alpha \leq 8°$ the biplane configuration with $x_0 = 0$ shows significantly lower lift than the other configurations. In addition, the shockwave on the upper part of the two airfoils is in this configuration much larger.

At $M_\infty = 0.7$ and $M_\infty = 0.8$ the drag polar for $x_0 = 0$ is different than the other configurations. In Figure 6 the flow field for this biplane configuration shows choked flow, which is observed for $\alpha \geq 0°$. The flow velocity at the lower surface of the main-wing is increased and the lift of the main-wing decreases. In addition the drag increases as the shockwave length is increased.

Differences in the results between positive and negative stagger is small. At $M_\infty = 0.4$ negative stagger shows slightly higher lift per drag than positive stagger for $C_l \geq 1.5$. This is opposite to the results at $0.7 \leq M_\infty \leq 0.8$, where the positive stagger showed slightly higher lift per drag for $C_l \geq 2$.

Based on these results additional calculations were performed on the NACA0012 biplane. In Figure 17-Figure 19 on page 1-1 the drag polar plots are shown for $x_0 = \pm 2, \pm 1, \pm 0.5, +0$ with $M_\infty = 0.6, 0.7, 0.8$ for $\alpha = 0°, 2°, 4°$. Interestingly no significant difference is observed between $x_0 = \pm 1$ and $x_0 = \pm 2$ at all Mach numbers, besides a change in effective angle of attack. That is, positive and negative staggered configurations seems to follow the same drag polar curve, but at different angles of attack.

At $M_\infty = 0.7$ the results for $x_0 = 0.5$ shows increased drag at $\alpha = 4°$. The flow field showed an increased shockwave on the main-wing compared to results with $x_0 = -0.5$. Both the shockwave on the upper and lower surface of the main-wing are located very close to the trailing edge.

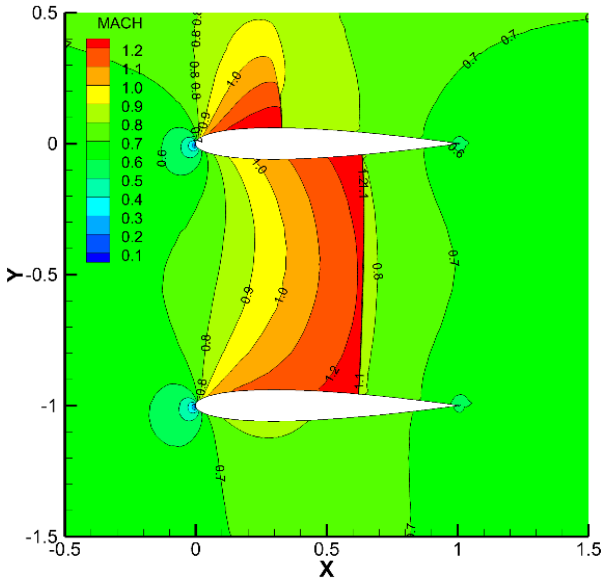

Figure 6. The flow field of the $x_0 = 0$ NACA0012 biplane configuration at $M_\infty = 0.7$ and $\alpha = 2°$ shows choked flow between the main-wing and truss.

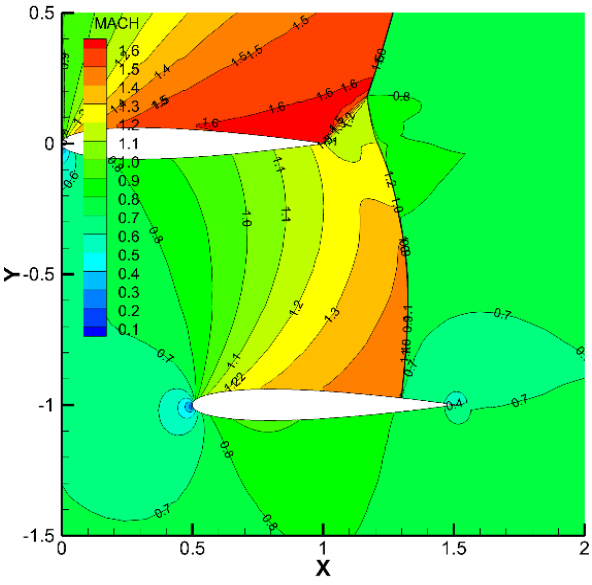

Figure 7. The flow field of the $x_0 = 0.5$ NACA0012 biplane configuration at $M_\infty = 0.8$ and $\alpha = 4°$ shows an oblique and a detached shockwave at the trailing edge of the main-wing.

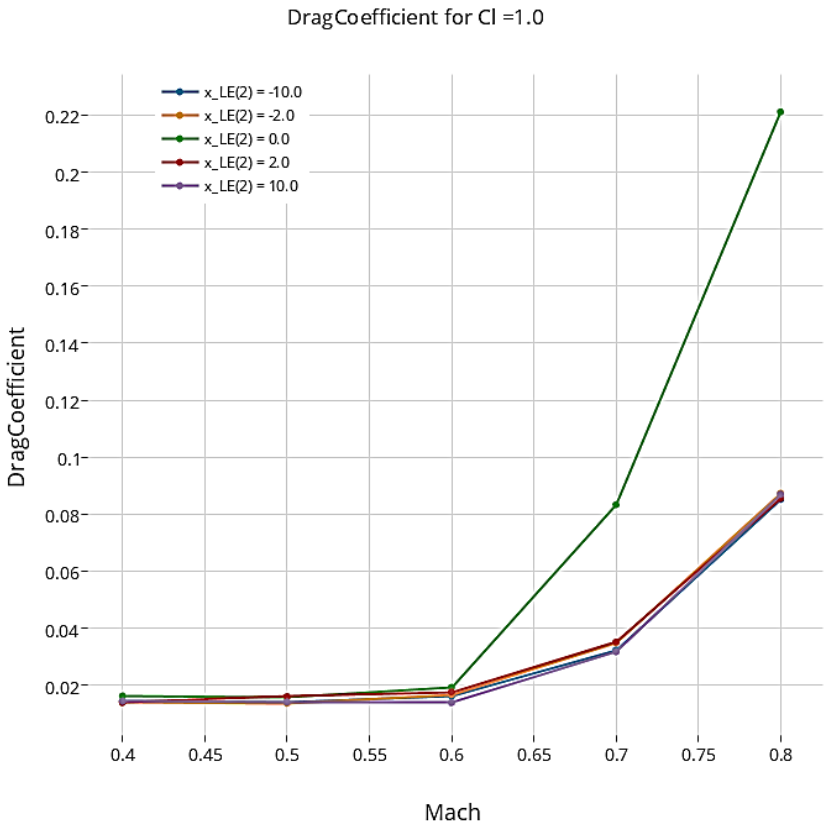

Figure 8. Drag coefficient the NACA0012 biplane at constant lift coefficient against Mach number.

At $M_\infty = 0.8$ the drag polar for $x_0 = \pm 0.5$ seems similar, but they show a shift in effective angle of attack since the results for $x_0 = -0.5$ at $\alpha = 4°$ are almost equal to the results for $x_0 = 0.5$ at $\alpha = 2°$. The flow field of the $x_0 = 0.5$ configuration shows an interesting flow pattern at $\alpha = 4°$ at $M_\infty = 0.8$ as is shown in Figure 7. The normal shock at the upper surface of the truss is connected to the normal shock originally found at the upper surface of the main-wing, but is now detached behind the trailing edge. In addition, an oblique shock is observed from the main-wing trailing edge towards the connected normal shock. This oblique shock is not refined by the presented grid refinement method, and introduces an error in this calculation of the aerodynamic coefficients.

The drag coefficients at constant lift are shown in Figure 8. Note that the combined drag and lift coefficients are shown from both the airfoils in the biplane configuration, which are nondimensionalised with c. Therefore these results must be compared with the single airfoil drag coefficient multiplied with 2. At subcritical flow conditions the drag is approximately $C_d \approx 0.015$, which is 2.5 times larger than the drag of the single NACA0012 airfoil. The biplane configurations with $x_0 = \pm 2, \pm 10$ show small differences in drag. At all Mach numbers the magnitude of the differences is equal, and is caused by the linear interpolation. The drag for the $x_0 = 0$ configuration however shows significant increase in drag for $M_\infty \geq 0.7$. The drag coefficient for zero stagger is almost 2.5 times larger than the drag of the $x_0 = \pm 2, \pm 10$ biplane at both $M_\infty = 0.7$ and $M_\infty = 0.8$.

RAE2822 Biplane

For the RAE2822 biplane the stagger was varied with $x_0 = \pm 1, \pm 0.5, \pm 0.25, 0$ and the gap was varied with $y_0 = -1.5,\ -1,\ -0.75,\ -0.5,\ -0.25$ in two separate studies. The drag polar plots for variable stagger are shown at Appendix II in Figure 20-Figure 24 on pages 1-1. At $0.4 \leq M_\infty \leq 0.6$ the differences are small, and again a shift in effective angle of attack is seen. At $M = 0.6$ and $\alpha = 8°$ the differences

become larger and flow separation at upper surface of the leading airfoil is observed.

For $M_\infty \geq 0.7$ the differences in the drag polar of the configurations are larger. At $M_\infty = 0.7$ and $0 \leq C_L \leq 1.5$ two groups of configurations can be identified with an almost equal drag polar. The first group consists of the $x_0 = 0$ and $x_0 = -0.25$ configurations. The results in this group are for $0° \leq \alpha \leq 2°$, and show choked flow in all these four configurations. The second group consist of the other configurations. They do not develop choked flow and have significantly lower drag. For higher lift coefficients the $x_0 = 0.25$ configuration shows a more rapid increase in drag as the angle of attack increases. The flow is not choked, but the shockwave on the truss is developed earlier. In addition, the shockwave on the main-wing is larger than in the other configurations.

At $M_\infty = 0.8$ the drag polar of $x_0 = 0$ and $x_0 = -0.25$ are again similar, but in contrast to $M_\infty = 0.7$ this similarity is observed for all investigated angle of attack. A shift in effective angle of attack for staggered configurations is again observed, showing a lower lift and drag for negative staggered configurations and vice versa, when compared to the zero stagger configuration. The flow field of the positive staggered configurations show an oblique shockwave at this velocity, similar to the NACA0012 biplane shown in Figure 7. One exception without an oblique shockwave is found: at $\alpha = 2°$ and $x_0 = 0.25$ the flow is still choked.

In Figure 9 the drag coefficients at constant lift are shown for the investigated staggered configurations. At $0.4 \leq M_\infty \leq 0.6$ the drag is $C_d \approx 0.01$, which is 2.5 times larger than the drag for a single RAE2822 airfoil. This is consisted with the difference in drag at subcritical flow conditions for the NACA0012 biplane and single airfoil. At $M_\infty = 0.7$ the drag increases for the $x_0 = 0$ and $x_0 = -0.25$ configuration to $C_d \approx 0.04$.

At $M_\infty = 0.8$ the biplanes can be divided into four different groups. First the drag is highest for the $x_0 = 0$ and $x_0 = -0.25$ configurations with $C_d \approx 0.18$. At $C_d \approx 0.15$ and $C_d \approx 0.13$ the biplanes with $x_0 = -0.5$ and $x_0 = 0.25$ respectively form a second group. The third group consist of the $x_0 = -1$ and $x_0 = 0.5$ configurations with a drag of $C_d \approx 0.6$. The fourth group consist of the $x_0 = 1$ configuration only with $C_d \approx 0.05$. The angle of attack required to generate $C_l = 1.0$ is lower than $\alpha < 1°$ for all configurations. The flow field show a small oblique shock for the positive staggered configurations and thus the calculated drag at $C_l = 1.0$ is sufficiently accurate. For larger angle of attack the oblique shock becomes larger, decreasing the accuracy of those calculations.

The drag polar plots with variable gap are shown at Appendix II in Figure 25-Figure 29 on pages 1-1. When the flow is not choked, a decrease in lift is observed for increasing gap at all investigated angles of attack. At $M_\infty = 0.6$ the biplane with $y_0 = -0.5$ show increased drag and decreased lift, when compared with the $y_0 \leq -0.5$ configurations. At $M_\infty = 0.7$ and $M_\infty = 0.8$ the drag increases linear with decreasing gap, while the lift decreases linear with decreasing gap.

The drag coefficient at constant lift for the gap study are shown in Figure 10. At $0.4 \leq M_\infty \leq 0.5$ the drag is $C_d \approx 0.01$. For the $y_0 = -0.5$ the drag is slightly higher but the flow is still subcritical. The drag at $M_\infty = 0.6$ for $y_0 = -0.5$ increases to $C_d \approx 0.06$ while the other configurations do not show an increased drag. At $M_\infty = 0.7$ the configurations with $y_0 = -1.00$ and $y_0 = -0.75$ have a drag of $C_d \approx 0.04$ and $C_d \approx 0.08$ respectively. The drag for $y_0 = -0.5$ has increased approximately linearly with the Mach number to $C_d \approx 0.11$. At $M_\infty = 0.8$ the drag of all configurations has increased. The drag for $y_0 = -0.5$ is $C_d \approx 0.23$. The drag decreases linearly with $\Delta C_d \approx 0.02$ for every increment of the gap to $C_d \approx 0.14$ at $y_0 = -1.5$. The flow fields shows an increased Mach number between the main-wing and truss as the gap decreases, while the shockwave on the upper surface of the main-wing remains equal.

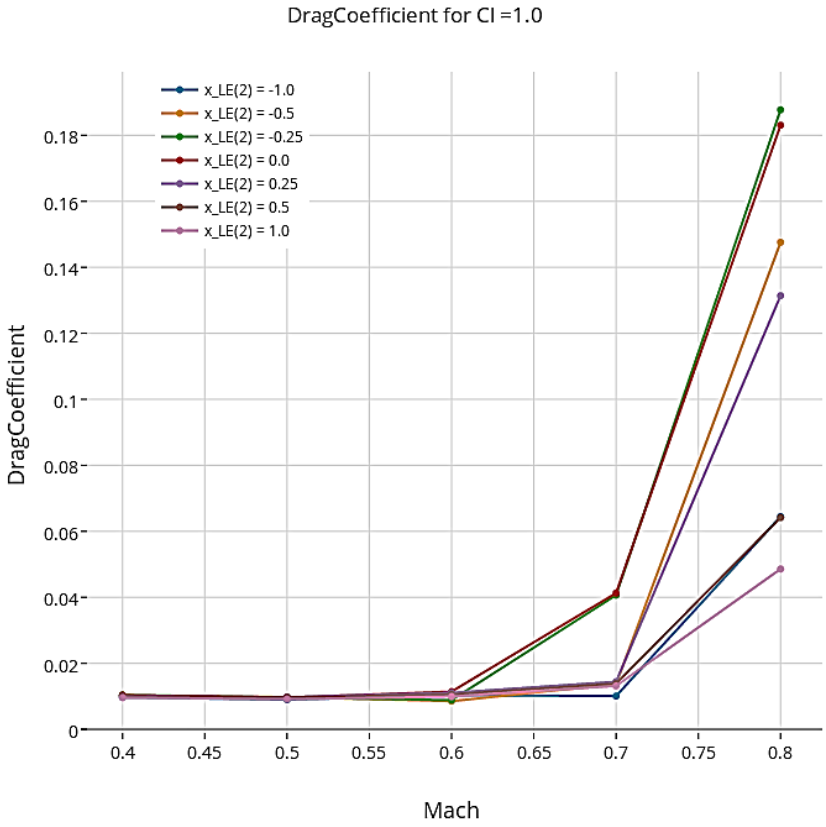

Figure 9. Drag coefficient the RAE2822 biplane at constant lift coefficient against Mach number for variable stagger.

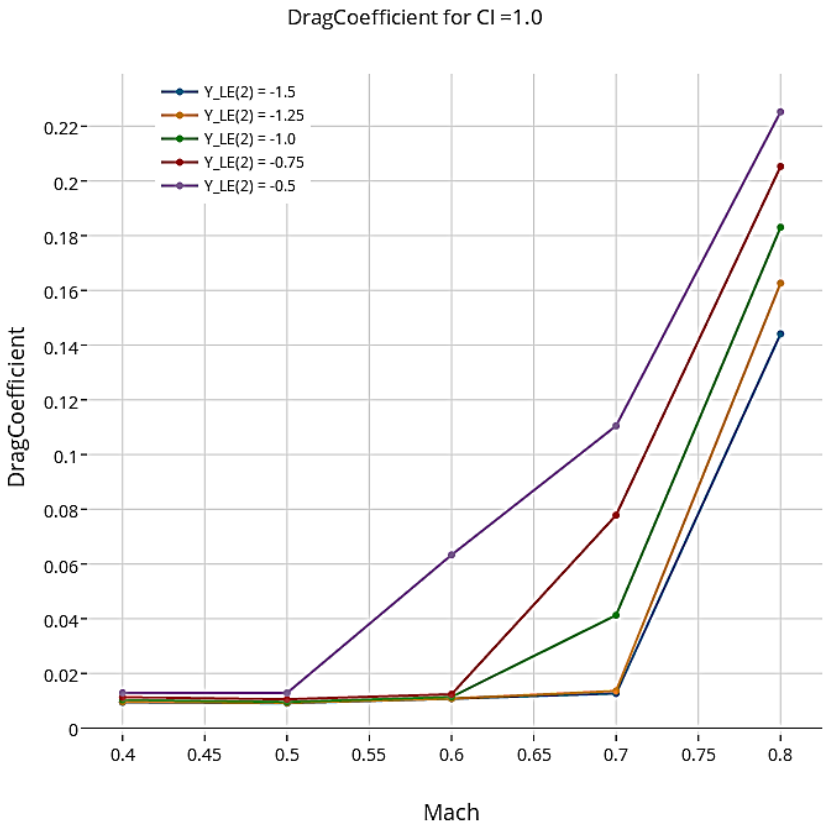

Figure 10. Drag coefficient the RAE2822 biplane at constant lift coefficient against Mach number for variable gap.

4. Discussion

Verification of flow solver

First the results of the test cases are compared with the results of other inviscid flow solvers presented by Vassberg (14). In Table 2 the 3-point Richardson extrapolation aerodynamic coefficients of the present method are shown, together with the percentage and absolute deviation from the mean of the other solvers. The shown results are the 3-point Richardson extrapolation with $h_w^c = 1.25E-3$, $h_w^m = 6.25E-4$ and $h_w^f = 3.125E-4$.

For the subcritical cases the theoretical drag in inviscid flow is zero. The calculated drag shows an absolute difference of less than 2 drag counts. The absolute difference for the lift- and moment-coefficient are lower than 0.002 and 0.0006 respectively. The percentage difference of the lift-coefficient is smaller than the moment coefficient at -1.01% and -22.8%. The drag at subcritical flow was calculated relatively poor with the present solver, as the percentage deviation is large. The results for the biplane and single airfoil calculations using a wall cell size of $h_w = 0.001$ therefore show relative large drag at subcritical conditions.

In the supercritical cases the theoretical drag is not zero. The calculated drag for the lifting and nonlifting case deviates 13 and 16 drag counts respectively. The percentage deviation of the drag in the non-lifting case is almost 20%, while all the aerodynamic coefficients of the lifting case are almost within 5% deviation. The lift is calculated within 0.01 absolute deviation and the drag within 0.0017 absolute deviation for both subcritical and supercritical cases. The observed differences in drag for variable stagger and gap are much larger, therefore the presented results in Figure 8, Figure 9 and Figure 10 are sufficiently accurate to observe flow transition from subcritical to supercritical flow.

The drag coefficient for $C_l = 1.0$ of the single NACA0012 and RAE2822 airfoil for subcritical cases was not zero, but $C_d \approx 0.006$ and $C_d \approx 0.004$ respectively. This difference is possibly caused by the different number of data points that was used to describe the airfoils, as the ratios are almost equal:

$$\frac{C_{d,RAE2822}}{C_{d,NACA0012}} \approx \frac{0.004}{0.006} = 0.67 \qquad (7)$$

$M_\infty = 0.5$	$\alpha = 0°$	$\alpha = 1.25°$		
CFD method	C_d	C_l	C_d	C_m
FLO82	+0.000000045	+0.180345850	+0.000000050	−0.002268812
OVERFLOW v2.1t	−0.000004058	+0.179777193	+0.000010030	−0.002262569
CFL3Dv6	−0.000000192	+0.179783519	+0.000012221	−0.002270588
CFL3Dv6+Vortex	–	+0.180351940	−0.000000134	−0.002277380
Mean	−0.000001051	+0.180064626	+0.000005542	−0.002269837
Present method	+0.000037826	+0.178248743	+0.000166499	−0.001752313
Percentage deviation	−3699.049%	−1.008462%	2904.31%	−22.8001%
Absolute deviation	0.000038877	0.0018159	0.000160957	0.000517524

$M_\infty = 0.8$	$\alpha = 0°$	$\alpha = 1.25°$		
CFD method	C_d	C_l	C_d	C_m
FLO82	+0.008342298	+0.356208937	+0.022684938	−0.038774022
OVERFLOW v2.1t	+0.008342171	+0.351662793	+0.022453440	−0.037946129
CFL3Dv6	+0.008341516	+0.348226045	+0.022501430	−0.037353559
CFL3Dv6+Vortex	–	+0.351596613	+0.022674853	−0.037838046
Mean	+0.008341995	+0.351923597	+0.022578665	−0.037977939
Present method	+0.009981671	+0.34369431	+0.023838316	−0.036268632
Percentage deviation	19.65568%	−2.338373%	5.578944%	−4.500789%
Absolute deviation	0.001639676	0.0082293	0.001259651	0.001709307

Table 2. The 3-point Richardson Extrapolation with $h_w^c = 1.25E-3$, $h_w^m = 6.25E-4$ and $h_w^f = 3.125E-4$ compared with the presented results by Vassberg (14) at both sub- and supercritical, and lifting- and nonlifting flow conditions.

$$\frac{\#_{RAE2822}}{\#_{NACA0012}} = \frac{12{,}802}{20{,}001} = 0.64 \qquad (8)$$

where $\#_{airfoil}$ indicates the number of data points used for the description of the airfoil. The reason why the number of data points only effects the drag at subcritical velocities is unknown.

The effect of stagger and gap

Three different flow patterns are observed for both the NACA0012 and RAE2822 biplanes, depending on the position of the airfoils and flow conditions. For $|x_0| \geq 1$ the generated lift of the airfoils influences the effective angle of attack of the individual airfoils as different shockwaves are observed. The resulting differences in the drag polar for these configurations are not negligible, but are small compared to the observed differences for the $|x_0| < 1$ configurations. Therefore they are not further considered in this study.

For the $|x_0| < 1$ configurations the transition towards from subcritical flow to supercritical flow is observed prior to the same transition of the single airfoils. This is consisted with results presented by Hwang et al. (16). The flow chokes between the two airfoils, as a two-dimensional duct is formed by overlapping sections of the inner surfaces of the airfoils. Two effects are observed in the drag polar of the NACA0012 biplane when the flow is choked. First the drag rises significantly at $\alpha = 0°, 2°$, because a shockwave is formed within the duct. Second the lift decreases at $\alpha = 4°, 6°, 8°$ because the flow expansion over the upper surface of the truss is limited by the main-wing and the flow expansion over the lower surface of the main-wing is increased. The duct thus lowers the lift of both the main-wing and truss. For the RAE2822 biplane the drag increases and the lift decreases simultaneously for $\alpha \geq 0°$, because lift is generated in all these configurations. For the RAE2822 biplane the $|x_0| = 0.25$ configurations were also investigated. Interestingly choked flow at $M_\infty = 0.7$ is observed only for the $x_0 = 0$ and the $x_0 = -0.25$, and not for the $x_0 = 0.25$, configurations at $\alpha = 0°$. To understand this the flow field of a single RAE2822 airfoil at $M_\infty = 0.7$ and $\alpha = 0°$ is shown in Figure 11. This flow condition is still subcritical for the RAE2822 single airfoil. An almost symmetric expansion on the upper surface and non-symmetric expansion on the lower surface is observed, with a symmetry line $R(x)$ at $R_{upper} \approx 0.46$ and $R_{lower} \approx 0.35$ on the upper and lower surface of the airfoil respectively. The non-symmetric expansion on the lower surface is inclined towards the leading edge because of the highly cambered aft section of the supercritical airfoil.

According to Anderson (17) the linearized small perturbation potential equation is valid for small angles of attack, slender bodies and $M(x, y) \leq 0.8$. Here $M(x, y)$ signifies the local Mach number at position (x, y). The linearized small perturbation potential equation can be recast into the Laplace equation through a simple coordinate transformation in the x-direction, and thus solutions can be superposed. Suppose that the solution for the RAE2822 airfoil at the same flow conditions, i.e. $M_\infty = 0.7$ and $\alpha = 0°$, is found for the linearized small perturbation potential equation and that it is equal to the solution the Euler equations from Figure 11. Define the Mach number perturbation δM as the local Mach number minus the free stream Mach number:

$$\delta M(x, y) = M(x, y) - M_\infty \qquad (9)$$

When superposing the Mach number perturbation of the two airfoils, the highest combined Mach number perturbation is

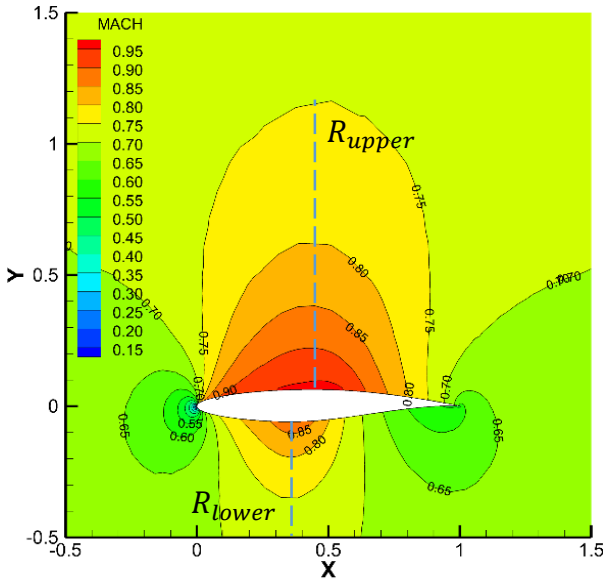

Figure 11. The flow field of the RAE2822 single airfoil at $M_\infty = 0.7$ and $\alpha = 0°$ shows a symmetric expansion over the upper surface, and a leading edge inclined expansion over the lower surface.

obtained when the symmetry lines of the expansions coincide:

$$\begin{aligned} x_0(\max C_d) &= R_{lower} - R_{upper} \\ &\approx 0.35 - 0.46 \\ &= -0.11 \end{aligned} \qquad (10)$$

This qualitative approximation matches with the obtained results, as it lies between the $-0.25 < x_0 < 0$ configurations that showed the lowest drag divergence Mach number.

For the $x_0 = 0.25$ and $x_0 = 0.5$ biplane configurations a detached shockwave at the trailing edge of the main-wing is observed at $M_\infty = 0.8$ for $\alpha = 4°$ and $\alpha \geq 2°$ respectively. In the flow pattern an oblique shock originating from the trailing edge of the main-wing connects to midpoint of the detached shockwave. At these flow conditions the flow in the duct continuous to expand until it reaches the trailing edge of the main-wing. The flow over the upper surface of the main-wing also expands until it reaches the trailing edge. Supersonic velocity at the upper surface of the trailing edge is decelerated through an oblique shock to the flow exiting the duct. A normal shock decelerates the supersonic region to subsonic velocity. The drag polar does not clearly show the transition from choked flow towards this flow pattern, and thus differences in drag and lift between choked flow and the detached shockwave are small.

The effect of gap was investigated for the RAE2822 biplane only. It was found that as the gap becomes smaller choked flow develops at lower free stream Mach number and the drag increases. The superpositioning method cannot be used be used to predict the gap at which the flow chokes. This is because of the following two reasons. Firstly, the linearized small perturbation potential equation is valid when the local Mach numbers in the flow are smaller than $M(x, y) \leq 0.8$. Superposed solutions to this equation can therefore never be used to predict solutions with $M(x, y) \geq 1$. Secondly, the solution contains a non-physical space, i.e. the airfoil, where mirror-imaging must be applied when superposed, similar to the Milne-Thomson circle theorem as elaborated by Batchelor (18).

5. Conclusions

The present multi-level approach to grid refinement combined with a strong-shock detection method was successfully used to investigate the effect of stagger on NACA0012 and RAE2822 biplanes. The method was validated with the results of other inviscid solvers.

It was observed that choked flow develops between two airfoils if they are positioned such that the overlapping surfaces forms a duct. The transition from subcritical to supercritical flow, i.e. choked flow, occurs at flow conditions which are subcritical for the single airfoil. The choked flow reduces the lifting capabilities of both the main-wing and truss and increases the drag. Similar flow patterns for the TBW configuration are expected in the regions where the main-wing and truss connect. The results of the present study suggest that choked flow can be avoided if the stagger is larger than the truss chord length.

For increased Mach number the choked flow changed into to a new flow pattern, which is characterized by a detached normal shock and an oblique shock at the trailing edge of the main-wing. This flow pattern occurs when the flow through the duct and the flow over the upper surface of the main-wing reaches supersonic velocity at the trailing edge. The supersonic flow at the upper surface of the trailing edge than decelerates to the supersonic flow exiting the duct through an upward angled oblique shockwave. The detached normal shock connects to the truss upper surface. Changes in the drag polar due to the transition to the detached normal shock were small compared to the transition to choked flow.

The superposition principle was successfully used to calculate a qualitative approximation of the stagger of the RAE2822 biplane with the lowest drag divergence Mach number.

In future work it is advised to investigate the aerodynamic interaction with smaller increments in both the Mach number and angle of attack. The angle of attack should be limited to $\alpha_{max} = 6°$, because the maximum lift-to-drag ratio was found at $\alpha \approx 4°$ In addition, negative angles of attack should be included in the study to calculate the zero lift condition. The aerodynamic coefficients of the individual airfoils should be analysed to confirm the loss

of the lifting capabilities of the truss and main-wing due to choked flow.

References

1. *Multidisciplinary Design Optimization of Medium-Range Transonic Truss-Braced Wing Transport Aircraft.* **Meadows, N.A., et al.** 6, 2012, Journal of Aircraft, Vol. 49.

2. **Boeing.** Boeing 2014 Environment Report. [Online] 2014. [Cited: 7 May 2015.] http://www.boeing.com/aboutus/environment/environment_report_14/2.3_future_flight.html.

3. **SANDIN, R.C LLMAS.** *Aircraft Having A Lambda-Box Wing Configuration. US 011/0180660A1* United States, 2011.

4. *Aerodynamic Analysis of the Truss-Braced Wing Using Vortex-Lattice Superposition Appoach.* **Ting, E., et al.** 2014, 32nd AIAA Applied Aerodynamics Conference.

5. *Locally Implicit Total-Variation-Diminishing Schemes on Unstructured Triangular Meshes.* **Hwang, C.J. and Liu, J.L.** 10, 1991, AIAA Journal, Vol. 29, pp. 1619-1626.

6. *Multidisciplinary Design Optimization of a Truss-Braced Wing Concept.* **Nam, T., et al.** 2014, 14th AIAA Aviation Technology, Integration, and Operations Conference.

7. *Analysis of the Effect of Cruise Speed on Fuel Efficieny and Cost for a Truss-Braced Wing Concept.* **Chakraborty, I., et al.** 2014, 14th AIAA Aviation Technology, Integration and Operations Conference.

8. *High Reynolds Number Steady State Flow Simulation using Immers Boundary Method.* **Takahashi, Y. and Imamura, T.** 2014, AIAA SciTech, Vol. 52nd Aerospace Sciences Meeting, pp. 13-17.

9. **Tamaki, Y.** *Development of Finite Volume-Based Higher Order Schemes for Unstructured Hierarchical Cartesian Grid.* 2015.

10. *On New Simple Low-Dissipation Scheme of AUSM-Family for All Speeds.* **Shima, Eiji and Kitamura, Keiichi.** Orlando, Florida : 47th AIAA Aerospace Sciences Meeting, 2009.

11. *An Adaptively Refined Cartesian Mesh Solver for the Euler Equations.* **Zeeuw, D. De and Powell, K. G.** 1993, Journal of Computational Physics, pp. 56-68.

12. *Shock wave visualization and identification based in the theory of characteristics from CFD data.* **Kanamori.** 2011.

13. *Factors of Safety for Richardson Extrapolation.* **Xing, T. and Stern, F.** 6, 2010, Journal of Fluids Engineering, Vol. 132.

14. *In pursuit of grid convergence, Part I: Two-dimensional Euler solutions.* **Vassberg, John C. and Jameson, Anthony.** 2009, AIAA Paper 2009-4114.

15. **Roskam, J. and Edward, C.** *Airplane Aerodynamics and Performance.* 1997.

16. *Locally Implicit Total Variation Diminishing Schemes on Unstructured Triangular Meshes.* **Hwang, C.J. and Liu, J.L.** 10, s.l. : AIAA, 1991, Vol. 29.

17. **J.D. Anderson, Jr.** *Fundamentels of Aerodynamics.* fifth. s.l. : Mc Graw Hill, 2011.

18. **Batchelor, G.K.** *An Introduction To Fluid Dynamics.* s.l. : Cambridge University Press, 1967. ISBN 0-521-66396-2.

19. **Anderson, J.D.** *Modern Compressible Flow.* s.l. : McGraw-Hill, 2002.

Appendix I. NACA0012 Biplane Drag Polar Plots

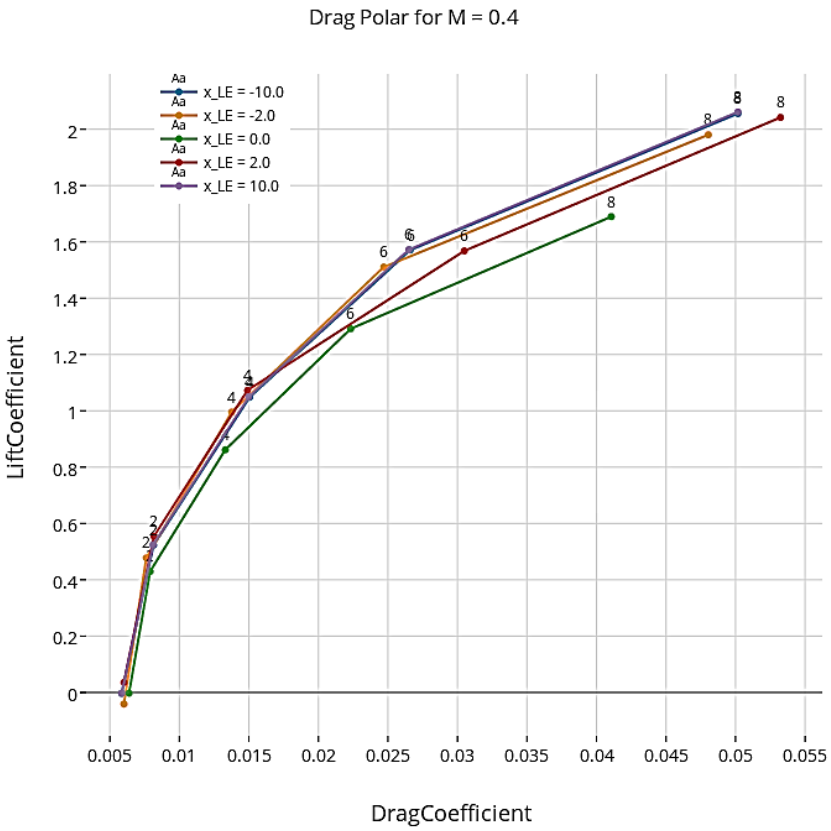

Figure 12. Drag polar of NACA0012 biplane at Mach 0.4

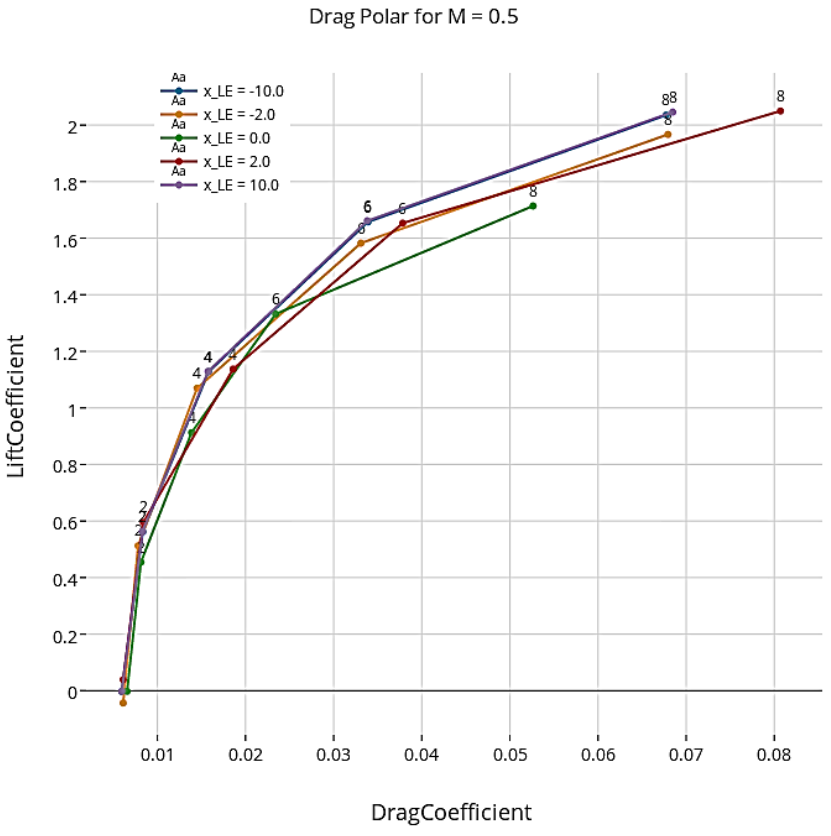

Figure 13. Drag polar of NACA0012 biplane at Mach 0.5

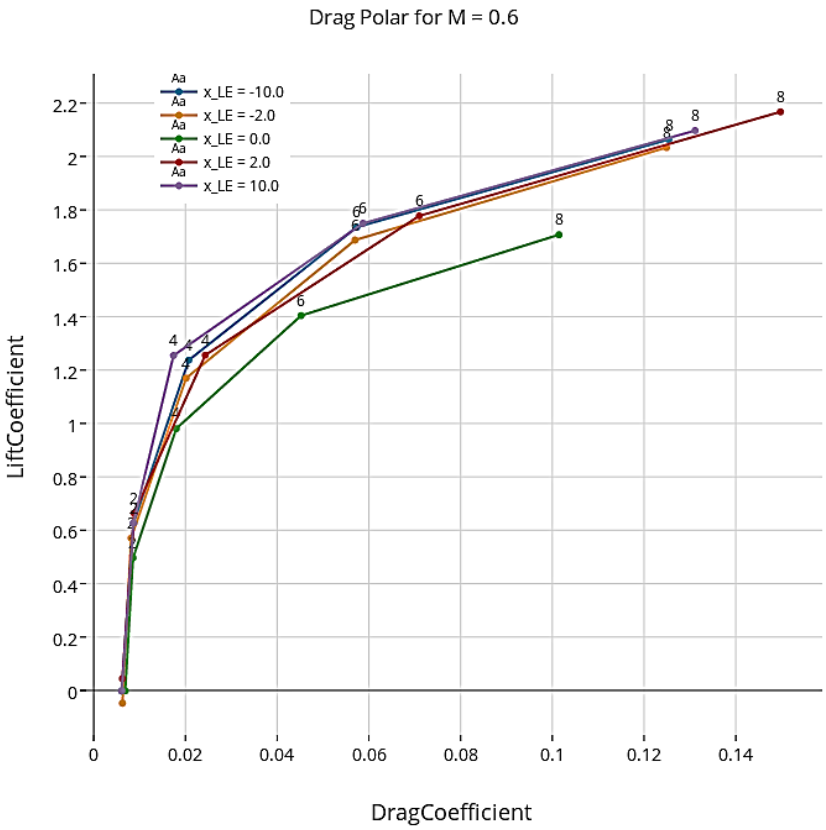

Figure 14. Drag polar of NACA0012 biplane at Mach 0.6

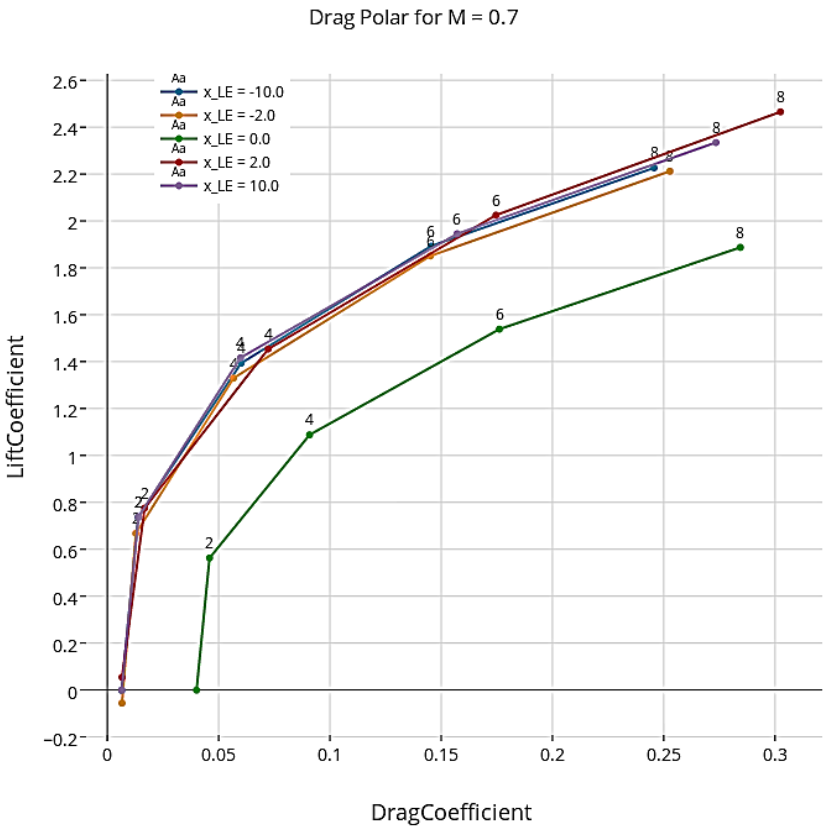

Figure 15. Drag polar of NACA0012 biplane at Mach 0.7

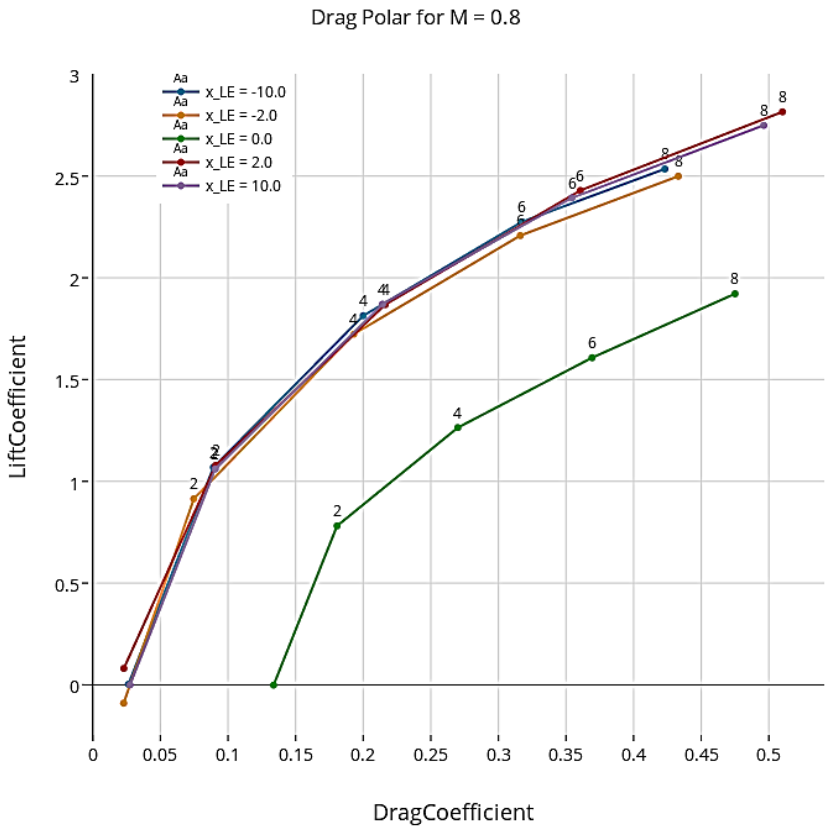

Figure 16. Drag polar of NACA0012 biplane at Mach 0.8

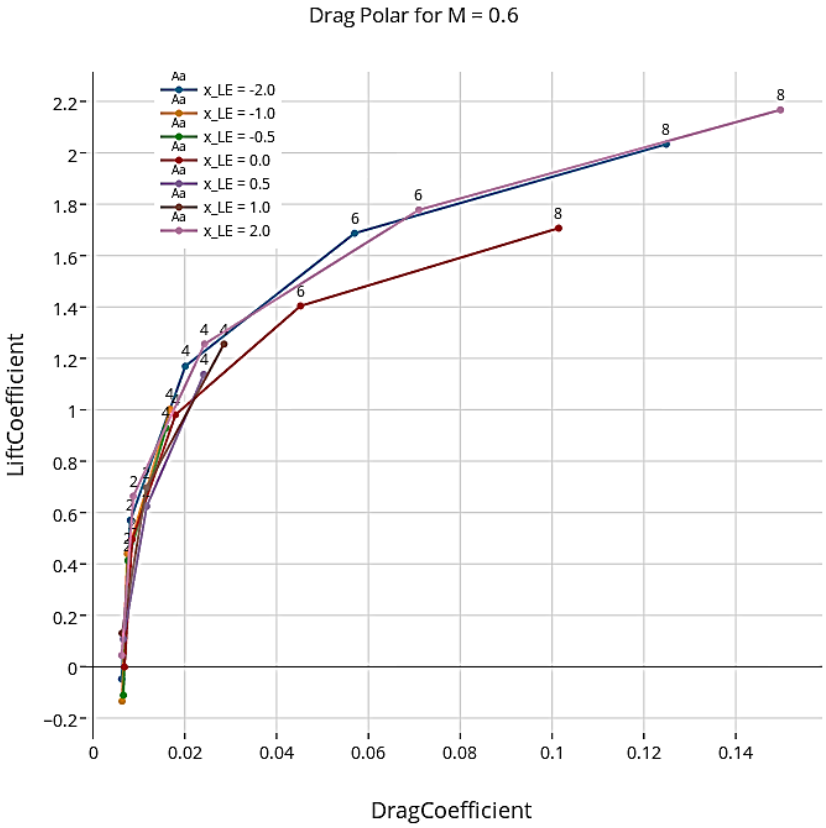

Figure 17. Drag polar of NACA0012 biplane at Mach 0.6 with small stagger increments

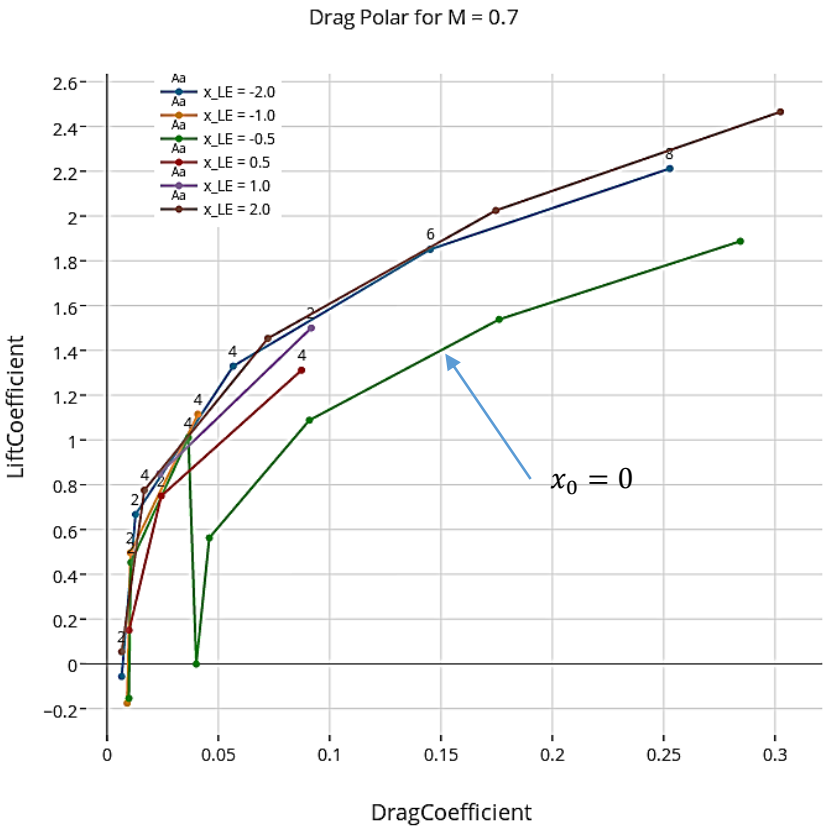

Figure 18. Drag polar of NACA0012 biplane at Mach 0.7 with small stagger increments

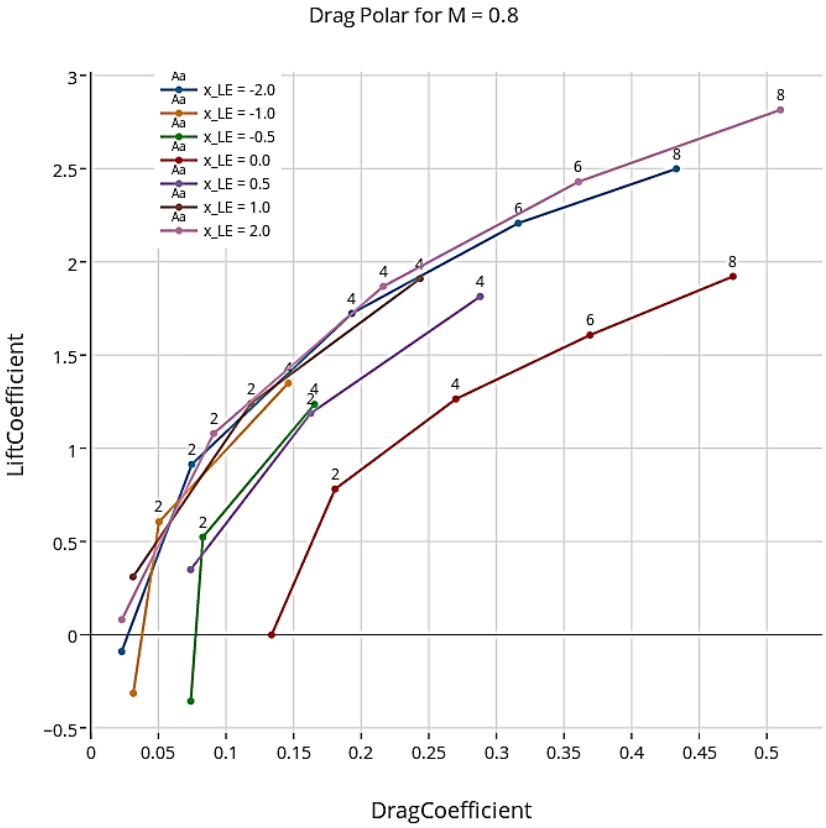

Figure 19. Drag polar of NACA0012 biplane at Mach 0.8 with small stagger increments

Appendix II. RAE2822 Biplane Drag Polar Plots

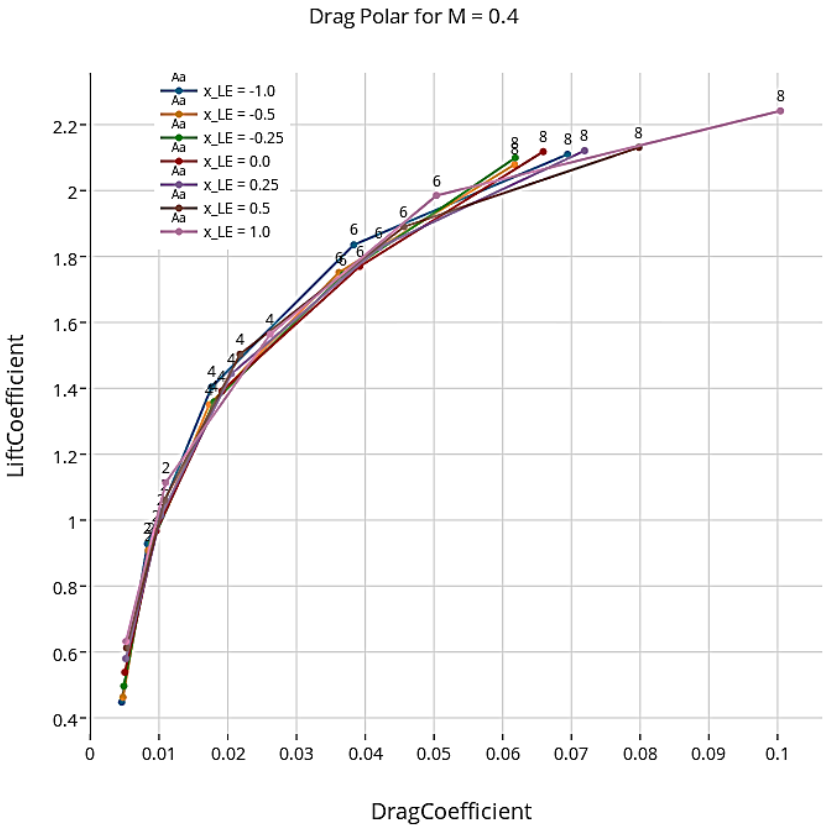

Figure 20. Drag polar of RAE2822 biplane at Mach 0.4 with variable stagger

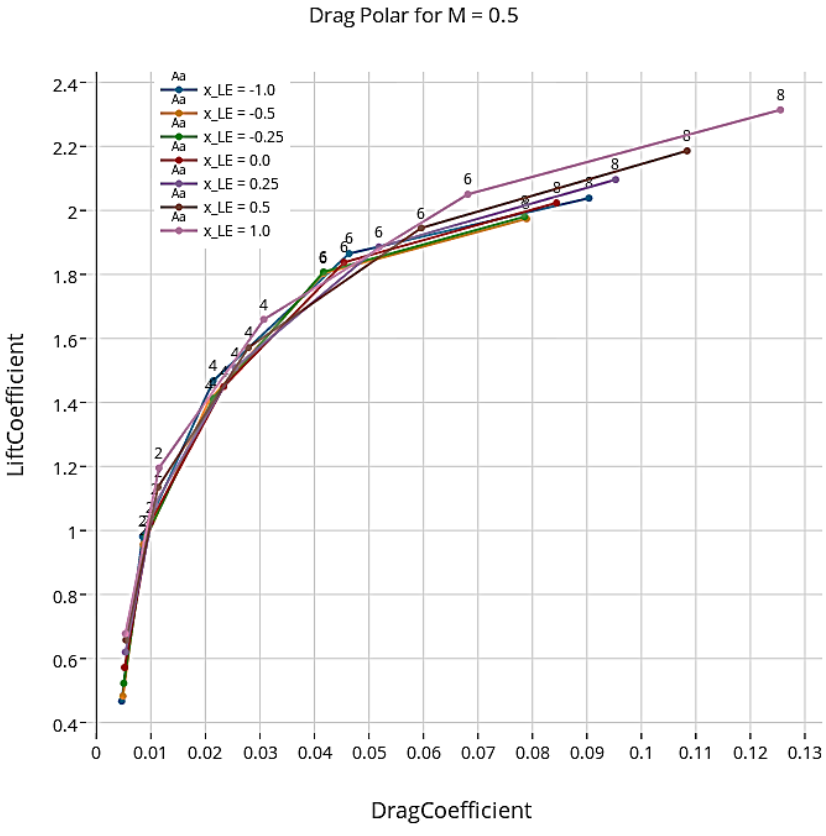

Figure 21. Drag polar of RAE2822 biplane at Mach 0.5 with variable stagger

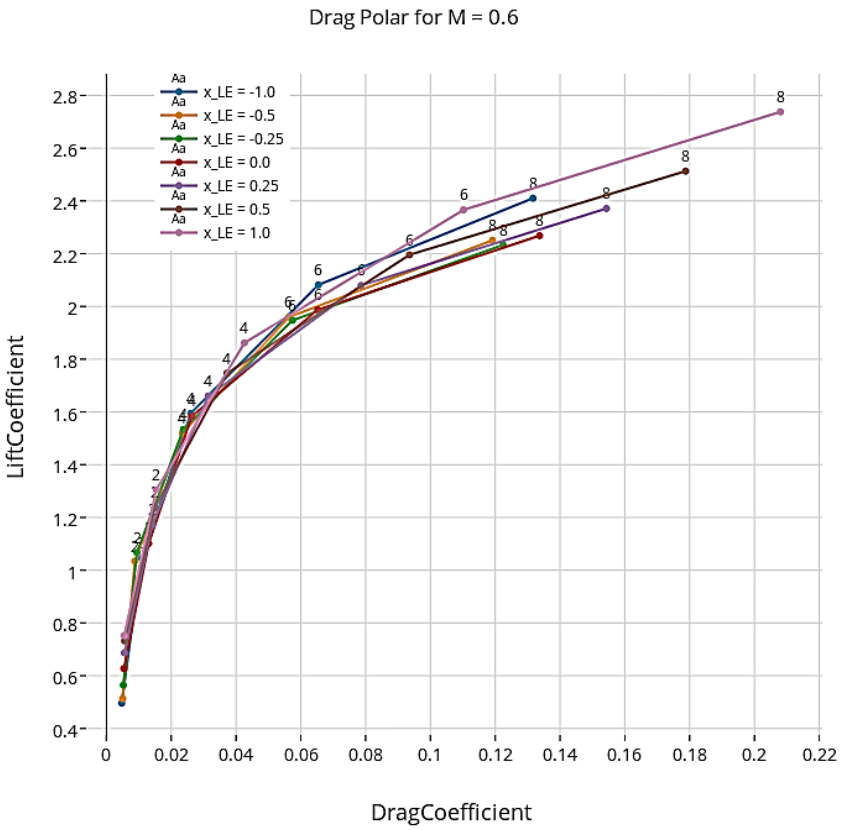

Figure 22. Drag polar of RAE2822 biplane at Mach 0.6 with variable stagger

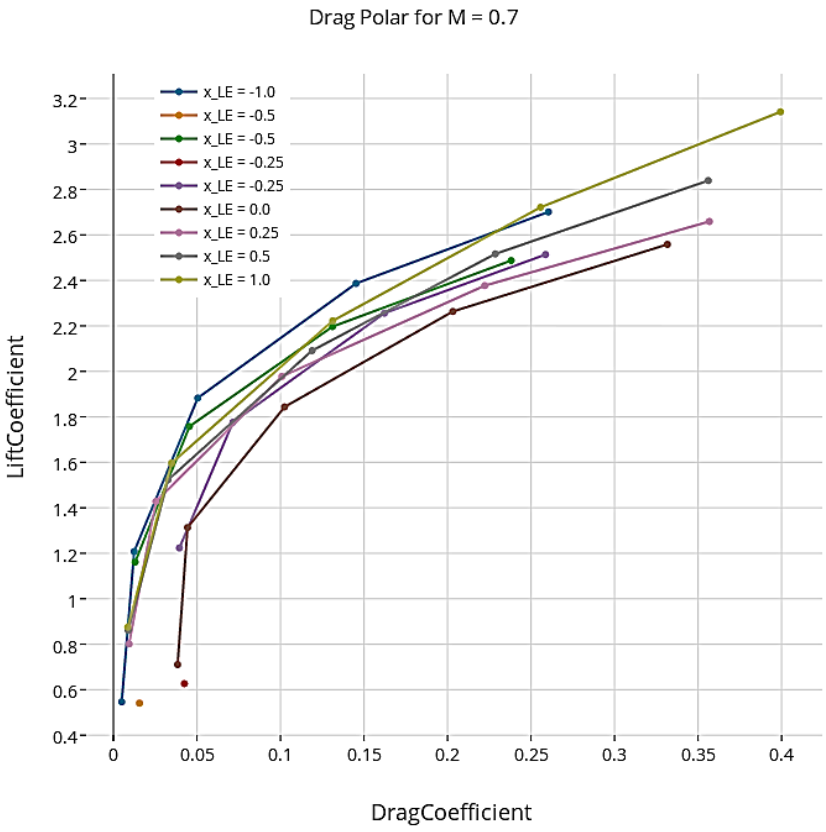

Figure 23. Drag polar of RAE2822 biplane at Mach 0.7 with variable stagger

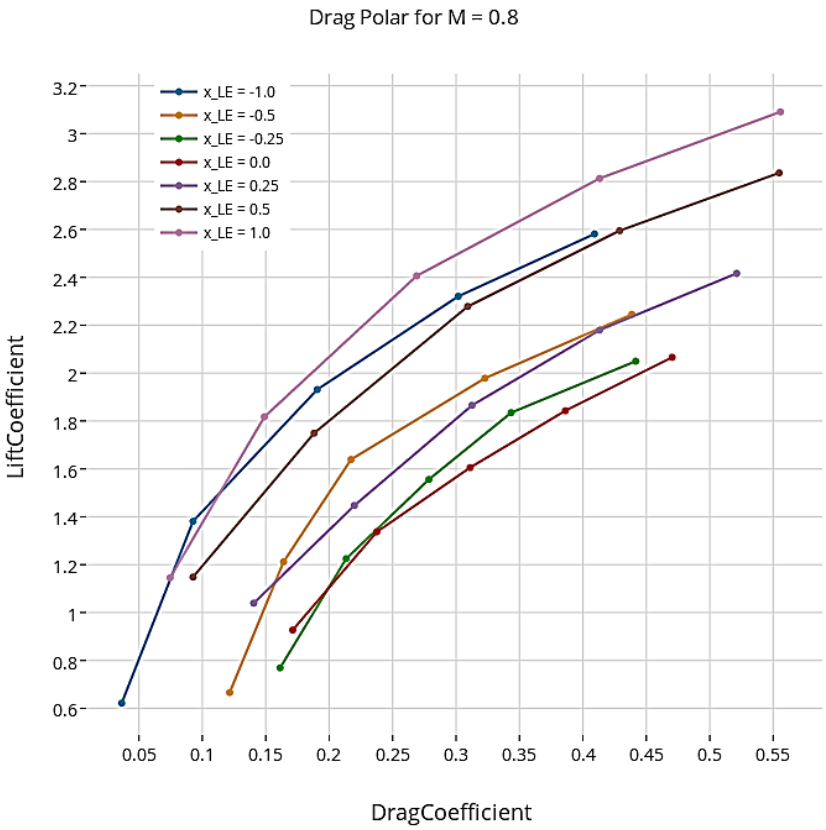

Figure 24. Drag polar of RAE2822 biplane at Mach 0.8 with variable stagger

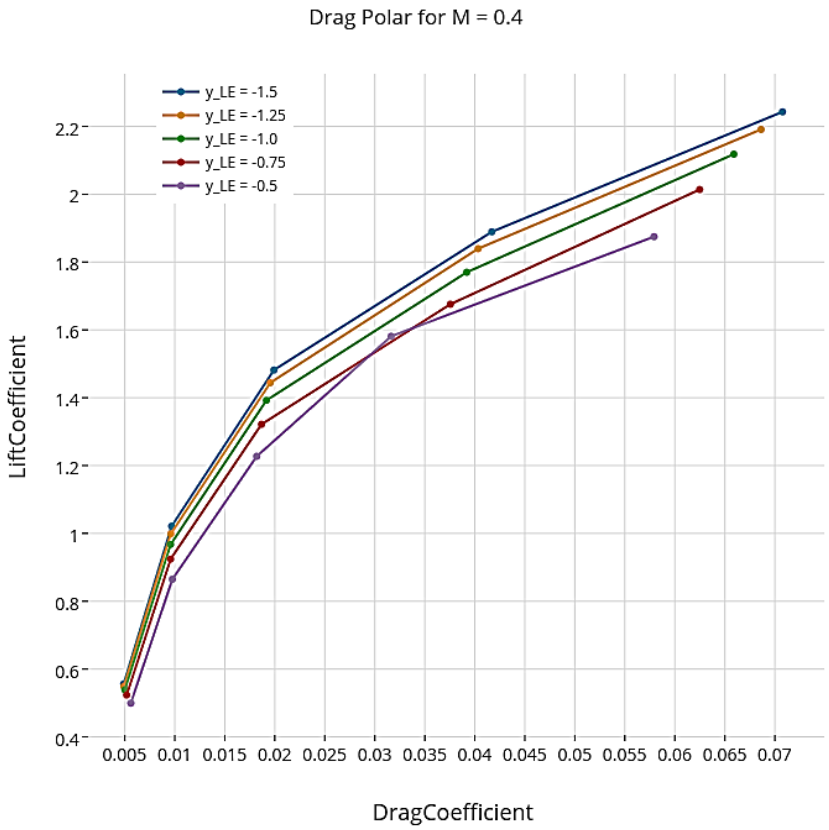

Figure 25. Drag polar of RAE2822 biplane at Mach 0.4 with variable gap

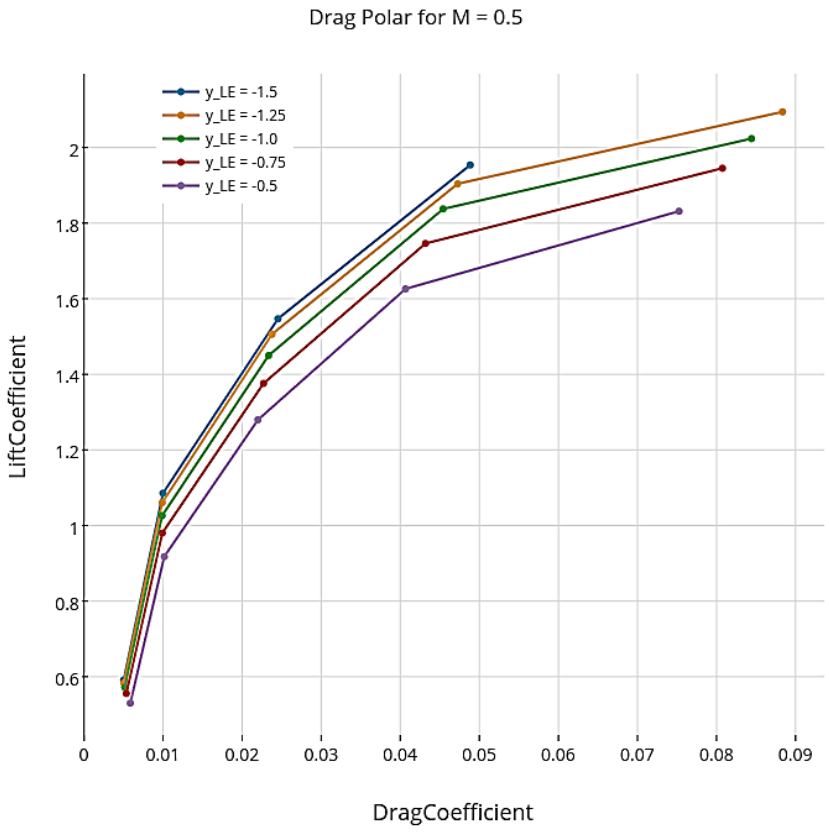

Figure 26. Drag polar of RAE2822 biplane at Mach 0.5 with variable gap

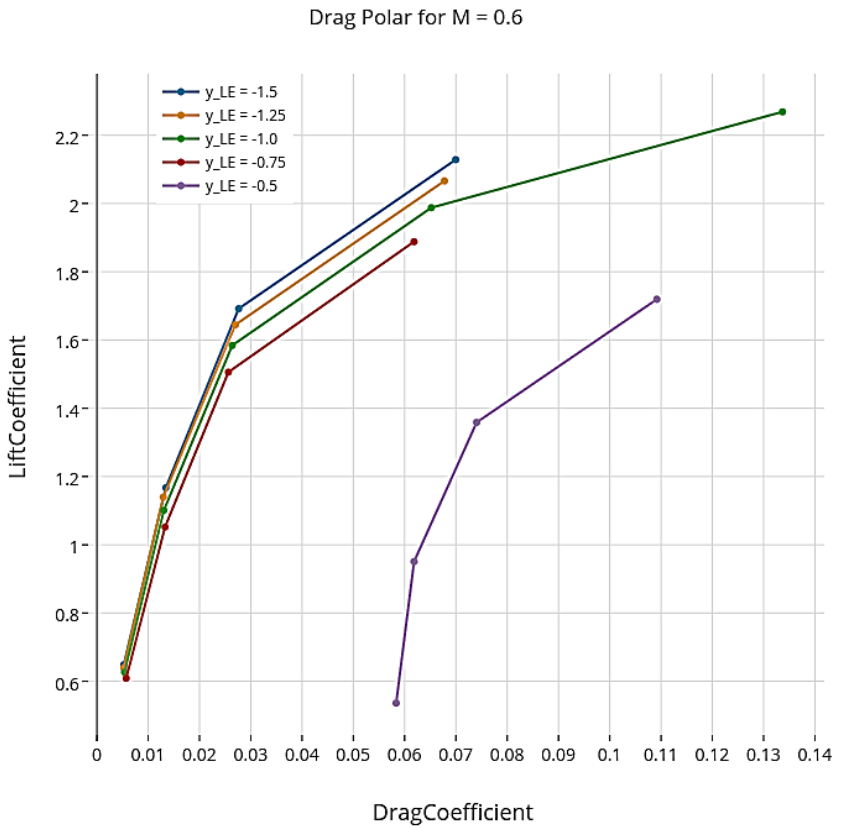

Figure 27. Drag polar of RAE2822 biplane at Mach 0.6 with variable gap

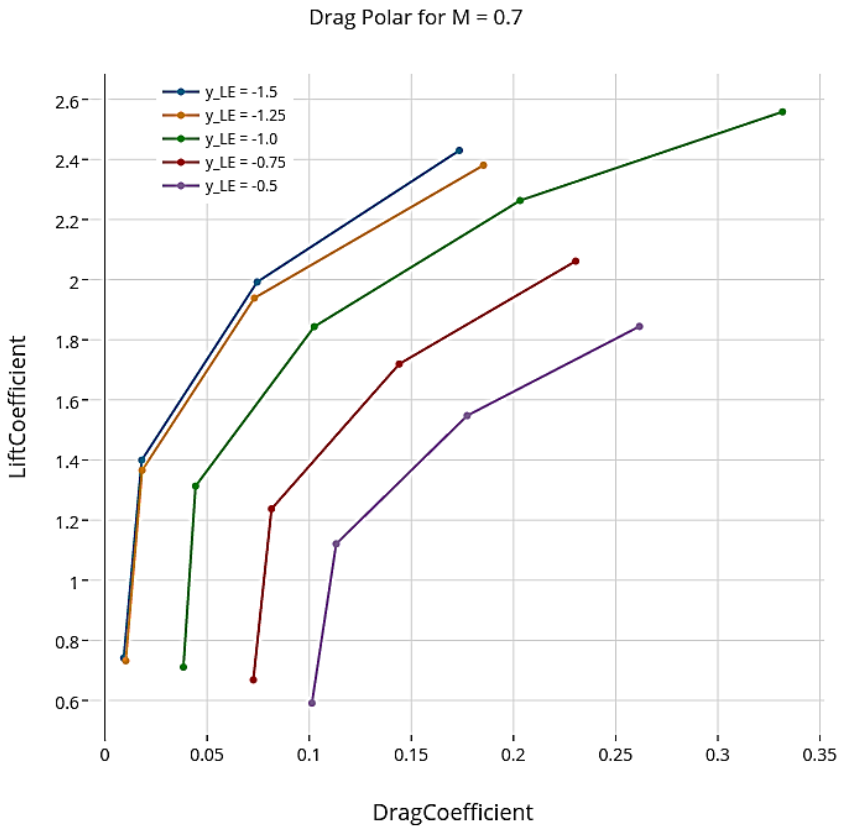

Figure 28. Drag polar of RAE2822 biplane at Mach 0.7 with variable gap

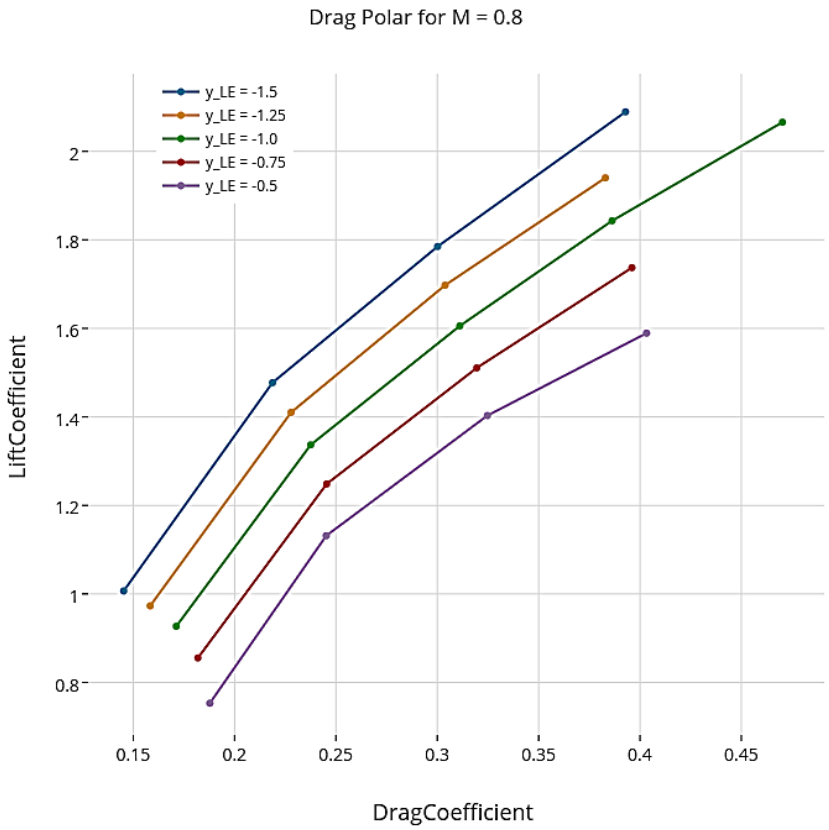

Figure 29. Drag polar of RAE2822 biplane at Mach 0.8 with variable gap